

Article

Comparative Study of Discrete PI and PR Controller Implemented in SRG for Wind Energy Application: Theory and Experimentation

Zeineb Touati ¹, Manuel Pereira ², Rui Esteves Araújo ^{2,*} and Adel Khedher ¹

- ¹ Ecole Nationale d'Ingénieurs de Sousse, LATIS—Laboratory of Advanced Technology and Intelligent Systems, Université de Sousse, Sousse 4023, Tunisia; zeineb.touati@eniso.u-sousse.tn (Z.T.); adel.khedher@eniso.u-sousse.tn (A.K.)
- ² INESC TEC and Faculty of Engineering, University of Porto, 4200-465 Porto, Portugal; up201205052@edu.fe.up.pt
- * Correspondence: raraujo@fe.up.pt

Abstract: The Switched Reluctance Generator (SRG) has been widely studied for Wind Energy Conversion Systems (WECS). However, a major drawback of the SRG system adopting the conventional control is the slow response of the DC link voltage controller. In this paper, a Proportional Resonant (PR) control strategy is proposed to control the output voltage of the SRG system to improve the fast response. The SRG model has a high non-linearity, which makes the design of controllers a difficult task. For this reason, the important practical engineering aspect of this work is the role played by the SRG model linearization in testing the sensitivity of the PR controller performance to specific parameter changes. The characteristics of steady-state behaviors of the SRG-based WECS under different control approaches are simulated and compared. The controller is implemented on a digital signal processor (TMS320F28379D). The experimental results are carried out using a 250 W 8/6 SRG prototype to assess the performance of the proposed control compared with the traditional Proportional Integral (PI) control strategy. The experimental results show that the PR control enhances the steady-state performance of the SR power generation system in WECS. Compared to PI control, the rise and settling times are reduced by 45% and 43%, respectively, without an overshoot.

Keywords: switched reluctance generator; wind energy generation; proportional integral control; proportional resonant control; voltage control; stationary state



Citation: Touati, Z.; Pereira, M.; Araújo, R.E.; Khedher, A. Comparative Study of Discrete PI and PR Controller Implemented in SRG for Wind Energy Application: Theory and Experimentation. *Electronics* **2022**, *11*, 1285. <https://doi.org/10.3390/electronics11081285>

Academic Editor: Raffaele Giordano

Received: 8 March 2022

Accepted: 16 April 2022

Published: 18 April 2022

Publisher's Note: MDPI stays neutral with regard to jurisdictional claims in published maps and institutional affiliations.



Copyright: © 2022 by the authors. Licensee MDPI, Basel, Switzerland. This article is an open access article distributed under the terms and conditions of the Creative Commons Attribution (CC BY) license (<https://creativecommons.org/licenses/by/4.0/>).

1. Introduction

The Wind Energy Conversion System (WECS) is becoming the fastest growing renewable energy source in the world and has attracted the interest of researchers and industries [1,2]. Following this trend, wind energy technologies are being expanded rapidly. Several studies related to Switched Reluctance Generators (SRG) in many applications have been presented in the literature, such as wind power generation systems [3], wave energy [4], aircraft [5], and electric or hybrid vehicles [6,7]. Nowadays, the SRG is a good candidate for wind turbine applications. It is attractive for this type of application because it has positive features, such as simplicity of construction, fault tolerance, low manufacturing cost, high performance, mechanical robustness, and absence of windings or permanent magnetic elements on the rotor [8–10]. In addition, SRG operates within a wide range of speeds at high-performance levels. Furthermore, SRG can be used to generate electricity without the necessity for a gearbox in wind turbine applications. For example, in [11], the authors present the design and operation of a dual-stator SRG for wind turbine applications. It can generate electricity with high efficiency in different wind directions. Based on experiments, it was verified that the efficiency of the generator is increased by 5 to 8% when the wind direction is reduced by 5°. The study is based on a generator with

a rated power of 2500 W and a torque of 70 Nm. The main limitations of SRG are the existence of large output voltage and torque ripples. However, they degrade the power generation performance. Many research efforts are currently being focused on reducing the output voltage variation, maximization of the SRG efficiency, and improving the voltage stabilization of SR power generation systems. In [12], the authors developed an SRG control for a low voltage DC grid based on a PI regulator. The authors have demonstrated that there is an optimal combination of control variables such as turn-on, turn-off angles, and the reference current, which maximizes the drive efficiency.

With same purpose, the authors in [13] describe a Direct Power Control (DPC) method. The DPC was designed to ensure the performance of the SRG over a wide range of speed. To improve the performance of SRG, the DPC was tested with a Proportional-Integral (PI) controller and a Sliding Mode (SM) controller. According to the experimental results, the SM controller showed better results than the PI controller. In [14], an improvement in SRG based on a traditional Proportional, Integral, and Derivative (PID) controller associated with a Maximum Power Point Tracking (MPPT) technique was presented. The performance of the machine was evaluated in terms of efficiency and torque ripple. The conventional PID controller has some advantages such as flexibility, simple structure, and low cost. Nevertheless, this controller has some drawbacks, especially when its parameters are not adjusted properly, particularly if the machine is non-linear. In [15], the authors demonstrate that over the traditional regulator PID, the SM controller can enhance the dynamic characteristics of SRG. However, the SM control technique has drawbacks when used with variable switching frequency, such as the chattering phenomenon and higher power losses. In [16], a freewheeling pulse train (FW-PT) control approach was proposed to reduce the voltage ripple. The experimental results confirm that, compared to the PID and pulse train (PT) strategies, the FW-PT control strategy can be used not only to suppress the output voltage ripple but also to achieve a faster response. In fact, the results with the FW-PT controller were promising, but the need of the predefined sets of control pulse combinations to be applied to each leg of the power converter results in increased switching power losses. In addition, the sets of preset pulse combinations are dependent on the topology of SRG.

As presented in [17], a PR and PI controller are applied to the DPC of three-phase 12/8 SRG to regulate the output DC voltage, despite the undesirable speed variations of WECS. Both controllers use the error between the measured power and reference, then calculate the turn-off angle. The results validate that the PR controller can reduce the power ripple when compared to the PI controller. In the mentioned reference, the PR controller has a better performance due to the reduction of ripple under all conditions. The power ripple is reduced by 27.77% when compared to the PI controller. Questioning the relative importance of the DPC solution compared to other solutions motivated revisiting the design of the DC bus voltage controller in order to compare it in terms of control variables and control laws. In what follows, we analyze the case where the controller calculates the reference current to extract all the energy from the wind with fast response and mitigate the overshoot of the DC bus voltage.

This paper presents a comparative study of a PI versus PR for DC voltage control. Theoretical aspects and comparative experimental results are discussed for both control laws. The main issue is to linearize the SRG model to find the optimal parameters of the controllers to ensure robust control. The results are validated and compared with the traditional regulator PI, as present in [18].

This paper has been organized as follows. Section 2 introduces the backgrounds of SRG. The design of voltage control using PI and PR controllers is described in Section 3, including the parameter tuning through frequency response. Section 4 discusses the discrete implementation of each controller. A comparison of experimental results is presented in Section 5 and the conclusions are addressed in Section 6.

2. SRG Backgrounds

2.1. Mathematical Model and Analysis of SRG Operation

The system used in this paper consists of a four-phase 8/6 SRG. The SRG is connected to the load, as given in Figure 1. The design of the switched reluctance machine essentially implies a laminate of magnetic material for the stator composition. The rotor is also laminated, such that both the stator and rotor have salient poles, without brushes. The absence of brushes on the rotor provides more robustness to this type of machine [19]. Consequently, the maintenance costs are reduced. The SRG has fault tolerance due to the independence between the magnetic fluxes of the SRG phases and the independence of the phases in the power converter [20]. The SRG system is operated by self-excitation based on a power converter four-phase asymmetric half-bridge circuit converter (AHBC). In the case of the self-excitation operation, the current flows from the SRG during the generation process and can be obtained as follows:

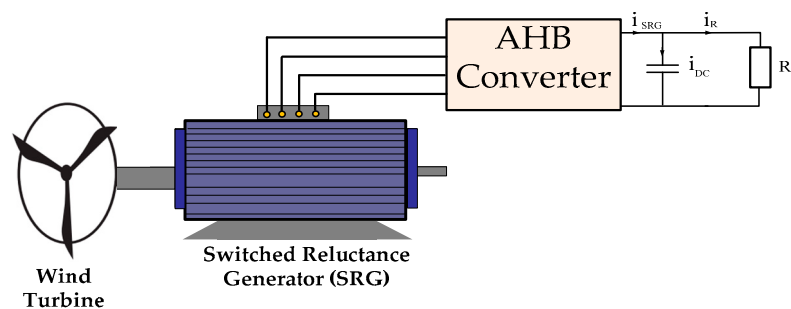


Figure 1. An overview of the system under study.

The voltage equation of SRG for the j th phase winding can be described as follows:

$$V_j = r_j i_j + \frac{d\phi_j(\theta, i_j)}{dt} \tag{1}$$

where i is the phase current, r is the phase resistance, and θ is the rotor position. Φ (Wb) is the concatenated stator flux per phase and is given by:

$$\phi_j(\theta, i_j) = L_j(\theta, i_j) \cdot i_j \tag{2}$$

L (H) is the inductance. It depends on the phase current and the rotor position. Therefore, the phase voltage, applying (1) and (2), is as follows:

$$V_j = r_j i_j + L_j(\theta, i_j) \frac{di_j}{dt} + i_j \omega_m \frac{dL_j(\theta, i_j)}{d\theta} \tag{3}$$

The electromotive force e is the last term of (3) and is given by:

$$e = i_j \omega_m \frac{dL_j(\theta, i_j)}{d\theta} \tag{4}$$

The electromagnetic torque can be determined based on the magnetic co-energy with respect to the rotor angular position as follows:

$$T(\theta, i) = \frac{dW_f(\theta, i)}{d\theta} = \frac{1}{2} i_j^2 \frac{dL_j(\theta, i_j)}{d\theta} \tag{5}$$

The mechanical expression of the SRG is described by:

$$T_e = T_M - B\omega_m - J \frac{d\omega_m}{dt} \tag{6}$$

where T_M is the generated turbine mechanical torque (Nm), T_E is the SRG electromagnetic torque (Nm), ω_m is the rotor mechanical speed (rad/sec), J is inertia moment ($\text{Kg}\cdot\text{m}^2$), and B is the viscous friction coefficient. Figure 2 shows an SRG drive; to highlight the principles of energy production, just one phase is shown as an example.

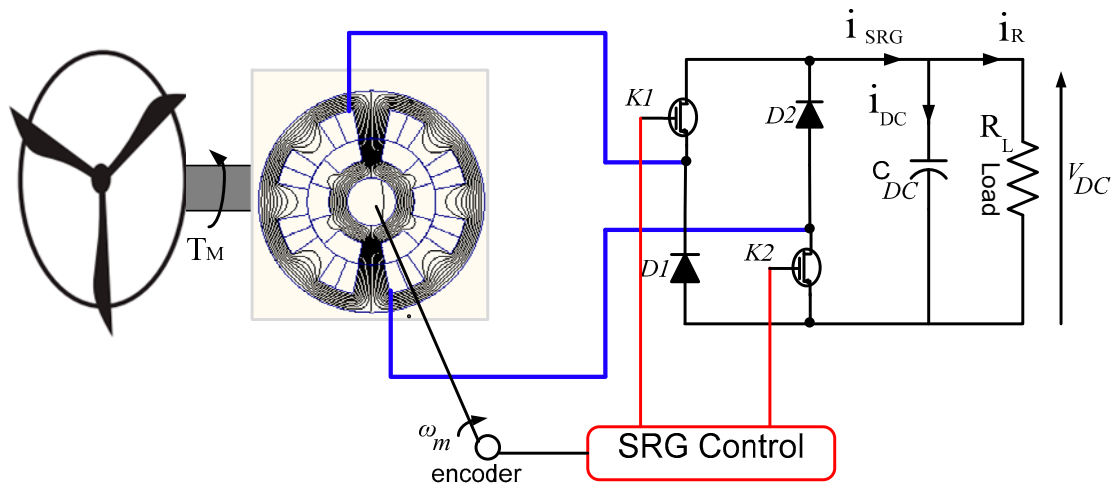


Figure 2. Principle of SRG operation.

Figure 3 shows all the states of the SRG operation [21]. Figure 3a presents an excitation state of SRG. The switches $k1$ and $k2$ of the converter are closed. The mechanical energy is transformed into magnetic energy and stored in the stator windings of the SRG. After excitation, the winding current flows through diodes $D1$ and $D2$, as shown in Figure 3b. The magnetic energy stored in the windings is transformed into electrical energy and transferred to the load. Figure 3c illustrates the freewheel operation through $D2$ and $k2$, which is called soft chopping.

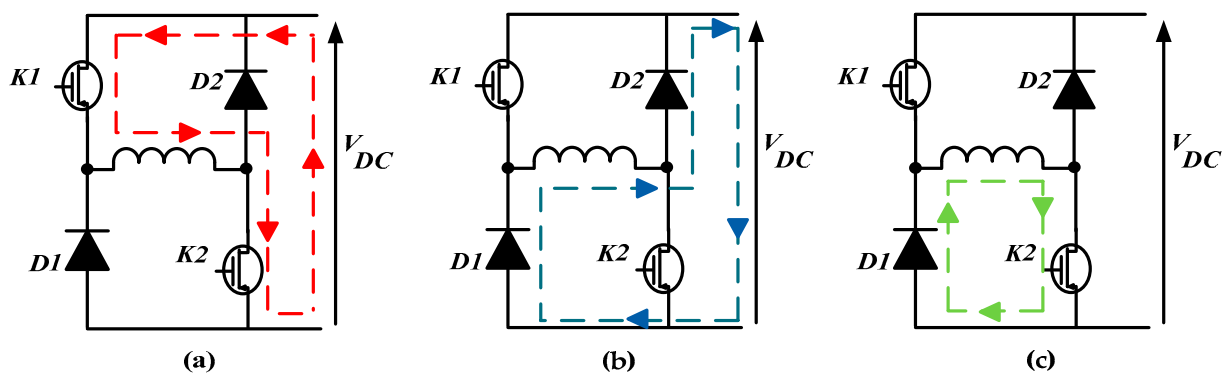


Figure 3. Operating states of switches: (a) excitation stage, (b) generation stage, and (c) fly-wheeling stage.

The flux linkage is not changed during the fly-wheeling chopping process. The voltage at the generator windings in the excitation and generation mode is given by:

$$V_j = \begin{cases} r_j i_j + L_j(\theta, i) \frac{di_j}{dt} + e \\ -r_j i_j - L_j(\theta, i) \frac{di_j}{dt} - e \end{cases} \quad (7)$$

The existence of a nonlinear inductance causes the irregular phase winding and the charge and discharge, periodically, of the parallel capacitor, resulting from a fluctuation of

the output voltage [22]. In the case of self-excitation, the current flows from the SRG during the power generation phase given by:

$$C_{DC} \frac{dV_{DC}}{dt} = C_{DC} \frac{dV_{DC}}{d\theta} \omega_m = i_{SRG} - i_R \tag{8}$$

where i_{SRG} is the generator current and i_R is the load current. The capacity voltage V_{DC} can be obtained from (9) as in [18]:

$$V_{DC} = C_1 e^{\frac{-\theta}{R_L C_{DC} \omega_m}} - R_L \int_{\theta_{on}}^{\theta_{off}} i_{SRG} d\theta \tag{9}$$

where C_1 is the integral constant, θ_{on} is the conduction angle, θ_{off} is the turn off angle, and R_L is the resistance of load. As can be seen, the output voltage V_{DC} is mainly affected by the parameters θ_{on} , θ_{off} , R_L , C_{DC} , and i_{SRG} . Based on finite element analysis (FEA), we have derived the magnetization characteristics of SRG to determine the electromagnetic torque equation. Figure 4 highlights the magnetization characteristics of the SRG used in this work.

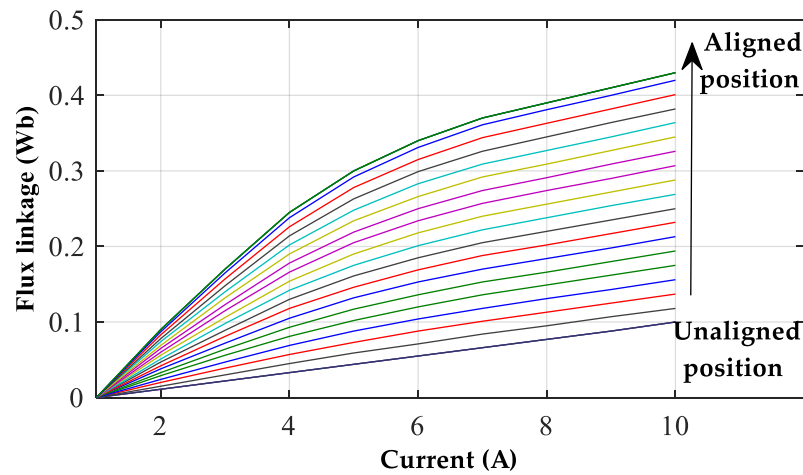


Figure 4. The 8/6 SRG magnetization characteristics versus current at different rotor positions.

2.2. Simplification and Linearization of SRG

Figure 5 shows the block diagram of the linearized SRG. A PI controller is used to control the current, and the power converter is modeled as a gain with a first-order delay, as follows.

$$E_{con}(s) = \frac{K_C}{1 + s T_C} \tag{10}$$

The gain of the power converter is given by:

$$K_C = \frac{V_{DC-nominal}}{V_{max}} \tag{11}$$

where V_{max} is the maximum control voltage. The time constant of the converter T_c is one approximation of the dead time of the power converter, the sampling, and signal processing. The sum of these very small time constants is approximated by:

$$T_C = \frac{T}{2} = \frac{1}{2f} \tag{12}$$

where f is the switching frequency of the converter. For more details, see references [18] and [23]. The transfer function of the current controller is given by:

$$\frac{\delta I(s)}{\delta V(s)} = \frac{B + sJ}{LJs^2 + (R_{eq}J + LB)s + (R_{eq}B + K^2)} \tag{13}$$

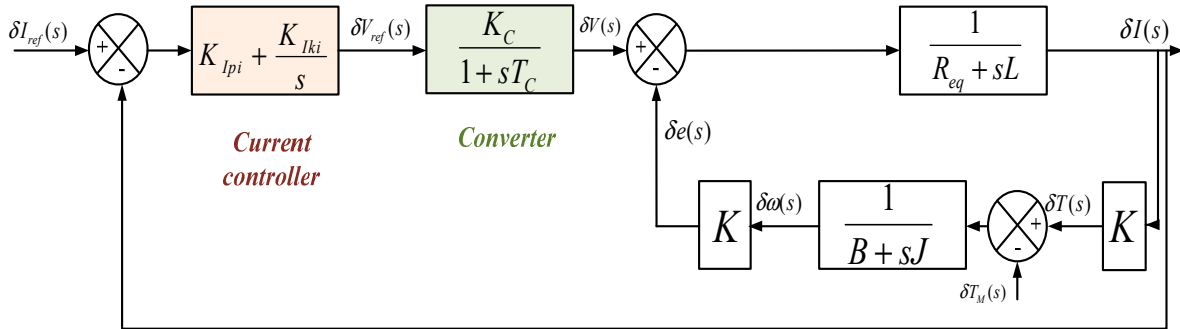


Figure 5. Schematic diagram of the linearized SRG with current control.

3. Voltage Controller Using PI and PR Controllers

The control strategy proposed in this section is based on regulating the voltage. Figure 6 shows the SRG voltage control block diagram. This way, the voltage controller processes the error between the measured voltage (V_{DC}) and its reference (V_{DC}^*). The main idea is to improve the performance of SRG using two different types of regulators, the PI and PR controllers. Typically, the voltage controller is implemented using a PI controller with voltage feedforward, as presented in Figure 7a. Instead, the PR controller can be applied as a voltage controller, as illustrated in Figure 7b. Compared to a PI controller, the only computational requirement that is imposed by the PR controller is an additional integrator for the second-order system implementation. For comparison, the PI and PR voltage controllers are analyzed.

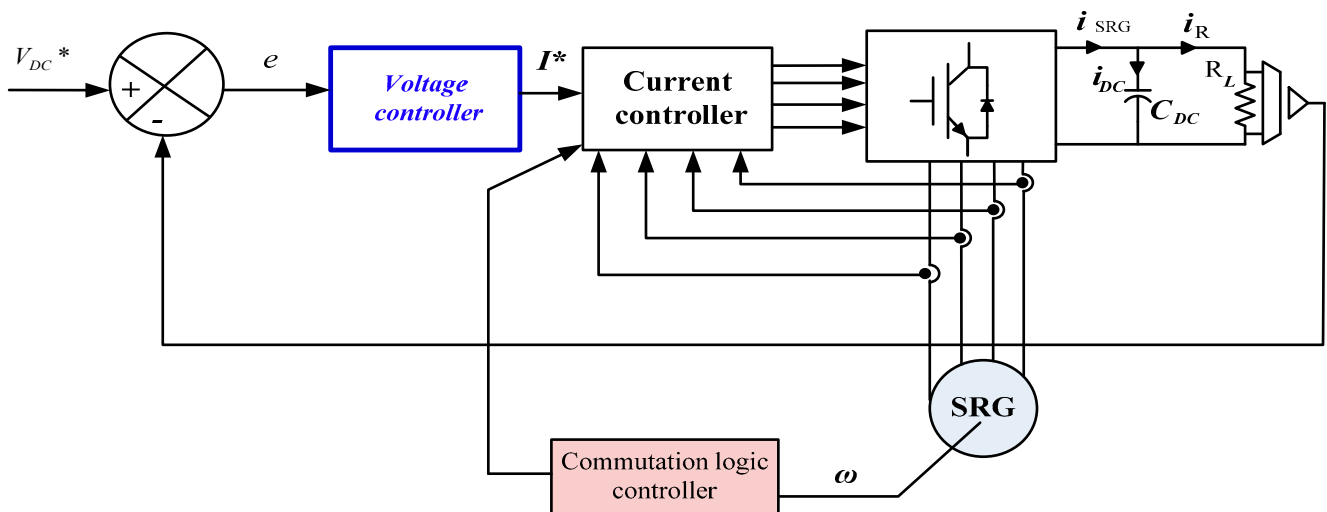


Figure 6. Proposed control strategy of SRG.

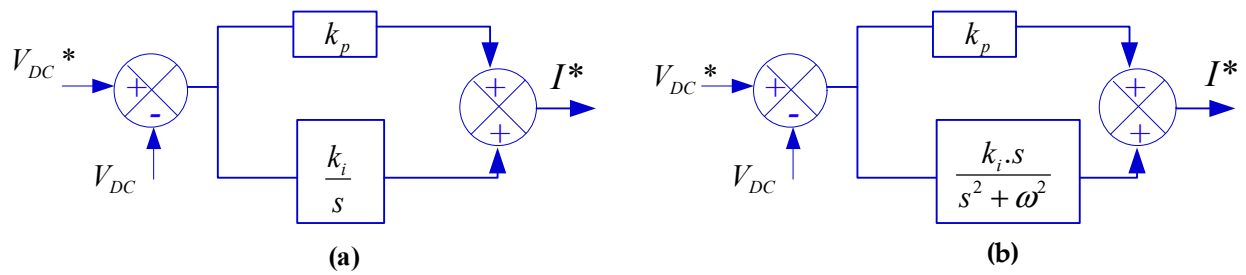


Figure 7. Voltage controller: (a) PI control; (b) PR control.

The equations of PI and PR voltage control used for the comparison are depicted in Equations (14) and (15).

$$G_{PI}(s) = k_p + \frac{k_i}{s} \tag{14}$$

$$G_{PR}(s) = k_p + R(s) = k_p + \frac{k_i s}{s^2 + \omega^2} \tag{15}$$

The reference current output (I^*) is next tracked by an inner current loop whose output is fed to a hysteresis control for switching the asymmetric half-bridge converter. The transfer function of closed-loop control can be determined only with the voltage controller and the load; the transfer function of the current closed-loop is approximated by a unit function. The closed-loop transfer function of DC link voltage based on PI and PR compensators is given by:

$$H_{PI}(s) = \frac{V_{DC}}{V_{DC}^*} = \frac{R_L \cdot (K_p s + K_i)}{R_L C_{DC} s^2 + (1 + R_L K_p) s + R_L K_i} \tag{16}$$

$$H_{PR}(s) = \frac{V_{DC}}{V_{DC}^*} = \frac{R_L K_p s^2 + \omega^2 R_L K_p s + R_L K_i}{R_L C_{DC} s^3 + (1 + R_L K_p) s^2 + R_L \omega^2 (C_{DC} + K_p) + (R_L K_i + \omega^2)} \tag{17}$$

The Bode diagram of the PI controller is presented in Figure 8. The frequency response is 1 kHz and the system phase margin is 78.4°.

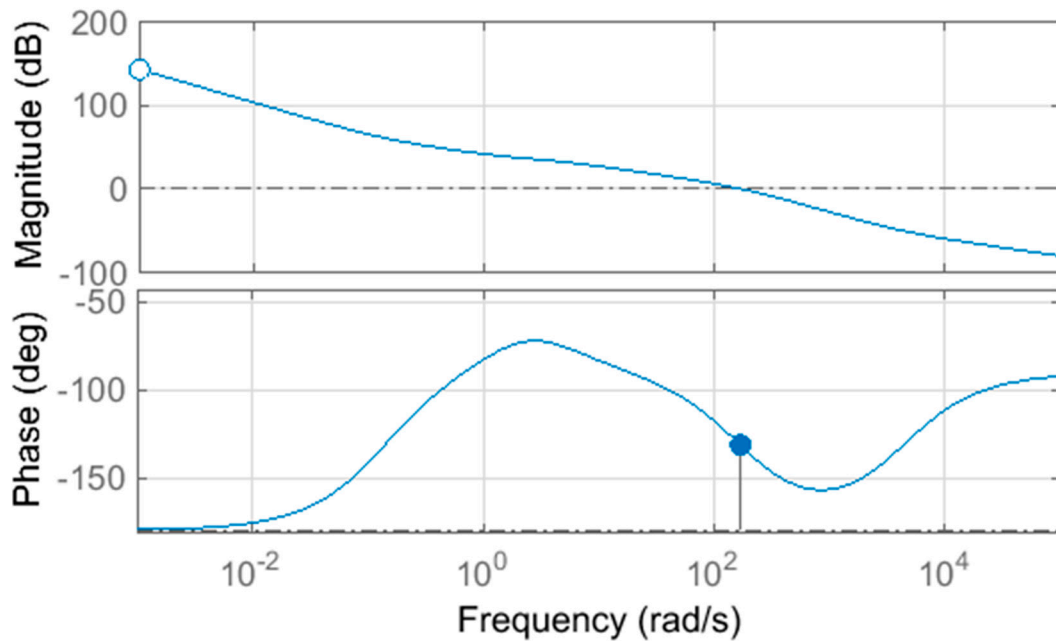


Figure 8. Bode diagram of closed-loop transfer function using PI controller ($K_i = 0.09$, and $K_p = 0.9$).

The tuning of the PR controller parameters is conducted by analyzing the stability using Bode diagrams and the phase margin. In order to study the effect of the PR controller parameters on the performance of voltage control, one parameter is changed while others are maintained constant. When $K_p = 100$ and the proportional gain K_i is changed, the magnitude of the PR controller rises, but the phase of the PR controller reduces, as illustrated in Figure 9.

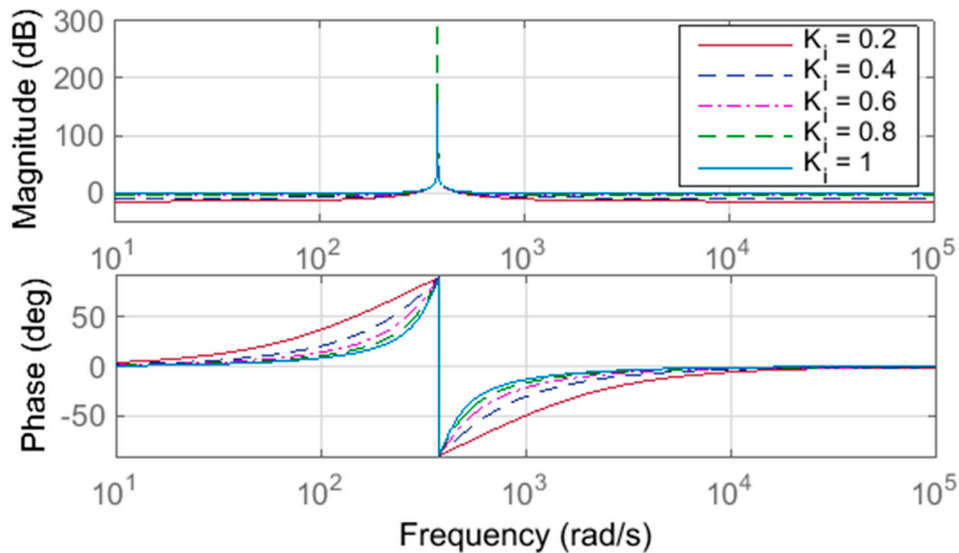


Figure 9. Frequency response of PR controller as a function of K_i changes.

Depicted in Figure 10 is the frequency response of the controller when K_p is added and K_i fixed at 1. It can be noted that the magnitude of the PR controller gain increases when K_p is added. The important results of this study should be highlighted. The parameters of the controller K_p and K_i are chosen to obtain a good closed-loop response and a steady state performance. The proportional gain constant K_i should be selected to ensure an improved tracking performance. A higher K_p value produces a faster response but increases the bandwidth and phase margin. Thus, the reasonable value of K_p can be selected according to the required bandwidth and phase margin. Based on the theoretical analysis, in this paper, the gains of the PR controller are taken as follows: $K_i = 1$, $K_p = 100$.

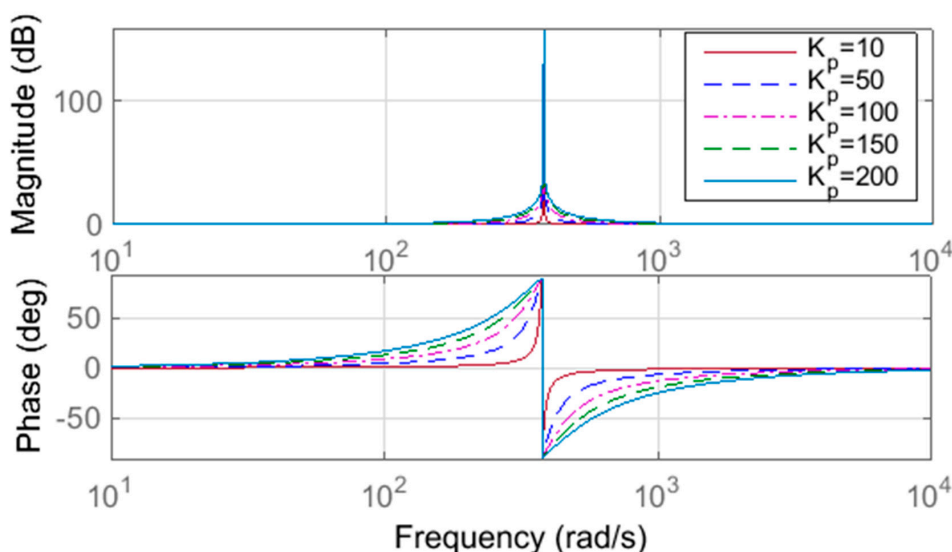


Figure 10. Frequency response of PR controller as a function of K_p changes.

4. Discrete Implementation

4.1. Implementation of PI Controller Using Discrete Transfer Function

The most widely used discretization method is the bilinear pre-normalized transform (Tustin) [24], which is defined as:

$$s = \frac{2}{T} \frac{(z - 1)}{(z + 1)} \tag{18}$$

where T is the sampling period and z is the forward shift operator. Equation (18) is substituted into Equation (14) and gives the following transfer functions in the z domain:

$$G_{PI}(z) = \frac{\left(k_p + k_i \frac{T}{2}\right) + \left(-k_p + k_i \frac{T}{2}\right) \cdot z^{-1}}{1 - z^{-1}} \tag{19}$$

$$G_{PI}(z) = \frac{Y(Z)}{E(Z)} = \frac{a_0 + a_1 \cdot z^{-1}}{1 - b_0 \cdot z^{-1}} \tag{20}$$

where

$$\begin{cases} a_0 = \left(k_p + k_i \frac{T}{2}\right) \\ a_1 = \left(-k_p + k_i \frac{T}{2}\right) \\ b_0 = 1 \end{cases} \tag{21}$$

For digital implementation, the differential equation of the PI controller is expressed in the difference Equation (22):

$$y(n) = a_0 \cdot e(n) + a_1 \cdot e(n - 1) + y(n - 1) \tag{22}$$

where $y(n)$ is the present output action of the controller, $y(n - 1)$ is the previous output control action, $e(n)$ is the present error, and $e(n - 1)$ is the previous error. Based on the PI controller parameters $K_p = 0.9$, $K_i = 0.09$, the coefficients of the digital PI controller with $T = 50 \mu s$ become $a_0 = 0.9$ and $a_1 = -0.9$.

4.2. Implementation of PR Controller Using Discrete Transfer Function

By using a bi-linear transformation, the discrete transfer function for the resonant term of Equation (15) is:

$$R(z) = \frac{k_i \cdot \frac{2}{T} \frac{(z-1)}{(z+1)}}{\frac{4}{T^2} \frac{(z-1)^2}{(z+1)^2} + \omega^2} \tag{23}$$

The relation $R(z)$ gives the following transfer function:

$$R(z) = 2 \cdot T \cdot k_i \frac{(1 - z^{-2})}{(4 + \omega^2 \cdot T^2) + (2 \cdot \omega^2 \cdot T^2 - 8)z^{-1} + (4 + \omega^2 \cdot T^2)z^{-2}} \tag{24}$$

where T is the sampling time. Equation (24) can be re-arranged in the present form:

$$R(z) = \frac{a_0(1 - z^{-2})}{b_0 + b_1z^{-1} + b_2z^{-2}} \tag{25}$$

where

$$\begin{cases} a_0 = 2 \cdot T \cdot k_i \\ b_0 = (4 + \omega^2 \cdot T^2) \\ b_1 = (2 \cdot \omega^2 \cdot T^2 - 8) \\ b_2 = (4 + \omega^2 \cdot T^2) \end{cases} \tag{26}$$

As a function of the error $E(z)$ and the controller output $U(z)$, the function of Equation (15) can be rewritten as:

$$G_{PR}(z) = \frac{Y(Z)}{E(Z)} = k_p + \frac{a_0(1 - z^{-2})}{b_0 + b_1z^{-1} + b_2z^{-2}} \quad (27)$$

The difference equation for the PR controller required for the DSP implementation is written in Equation (28):

$$y(n) = [a_0 \cdot (e(n) - e(n - 2)) - b_1 \cdot y(n - 1) - b_2 \cdot y(n - 2)]/b_0 + k_p e(n) \quad (28)$$

Using the same conditions for both controllers, e.g., reference voltage and required output speed, the performance of both controllers are studied in terms of execution time. In the discretization, the PR controller has two more products, two more sums, and three more data writes than the PI controller. The execution time for the PR speed controller is higher compared to the PI controller, as shown in Table 1. In the next section, we will discuss each controller in terms of performance and transient response (rise time, settling time, percentage overshoot) and robustness.

Table 1. Calculation of execution time.

Controller	Execution Time (μ s)
PI	0.66
PR	0.81

5. Experimental Results and Discussion

5.1. Experimentation

The proposed controller strategies are verified by experimental results achieved in a four-phase 8/6 SRG experimental platform, as illustrated in Figure 10. The parameters of SRG are given in Table 2. The SRG test bench was developed to perform the experiments and to obtain the results of this work. The diagram of the assembled system consists of an 8/6 four-phase SRG structure, encoder, SRG excitation rectifier, half-bridge converter, capacitor, load, digital signal processor (DSP), Texas Instrument TMS320F28379D, and induction motor, as shown in Figure 11.

Table 2. Database of 8/6 SRG.

Characteristics	Values
Output power	250 W
Maximum current	3 A
Inductance (aligned position)	0.14 H
Inductance (unaligned position)	0.021 H
Viscous friction	0.01 Nms
Moment of inertia	0.006 Kgm ²
Resistance of phase winding	5 Ω

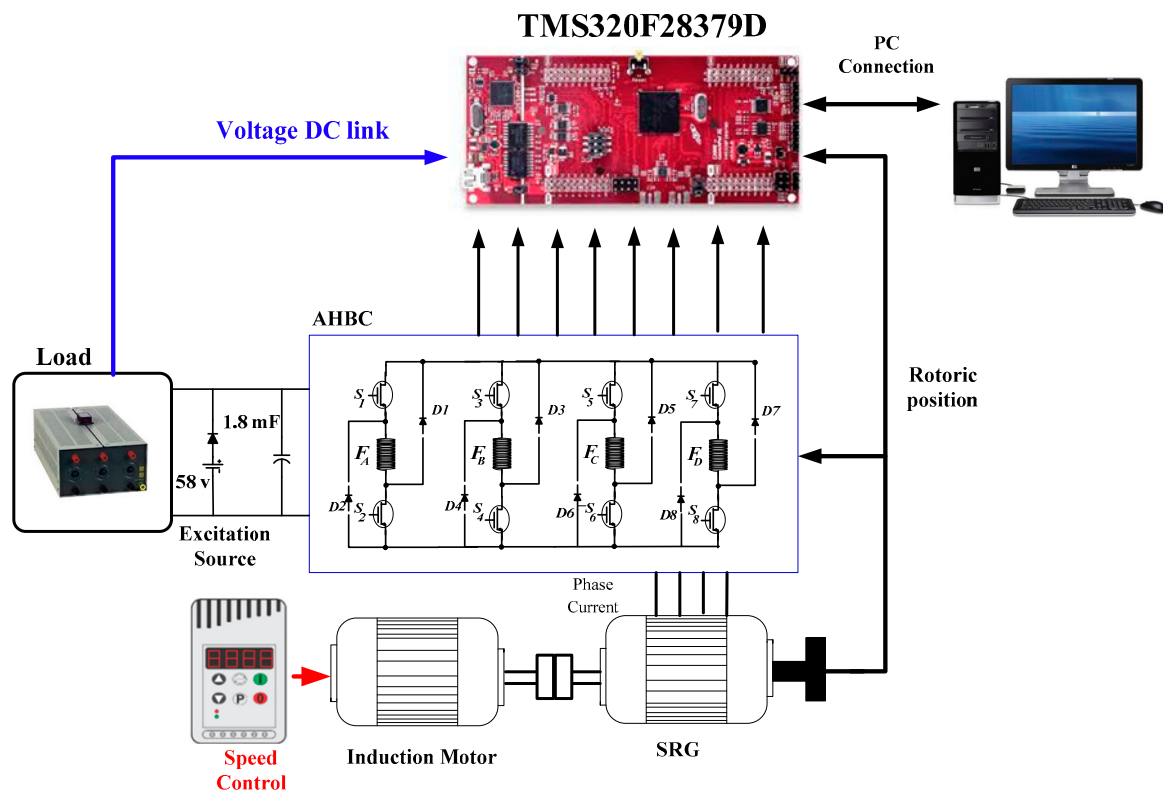


Figure 11. Experimental test bench.

5.2. Experimental Results and Discussion

The performance of both controllers is compared in terms of voltage ripple, steady-state response, peak overshoot, and rise time. The system has been tested under the following conditions: DC voltage excitation $V_{exc} = 58\text{ V}$, $R_L = 400\ \Omega$, and speed 600 rpm. The simulation and experimental parameters of regulators are shown in Table 3.

Table 3. Parameters of voltage regulators.

Parameters	Controller	
	PI	PR
Kp	0.9	100
Ki	0.09	1

To study the response of the SRG, a larger filter capacity is applied in the experiment and has a value of 1.8 mF. Figure 12 shows the output voltage of the two controllers (PI and PR). Figure 13 shows the waveforms of the DC link voltage V_{DC} , the phase current I_a , and the DC link current when the step response of voltage reference V_{DC}^* changes between 70 V and 83 V for the two methods of control. The current produced is 3A for both controllers, as shown in Figure 13.

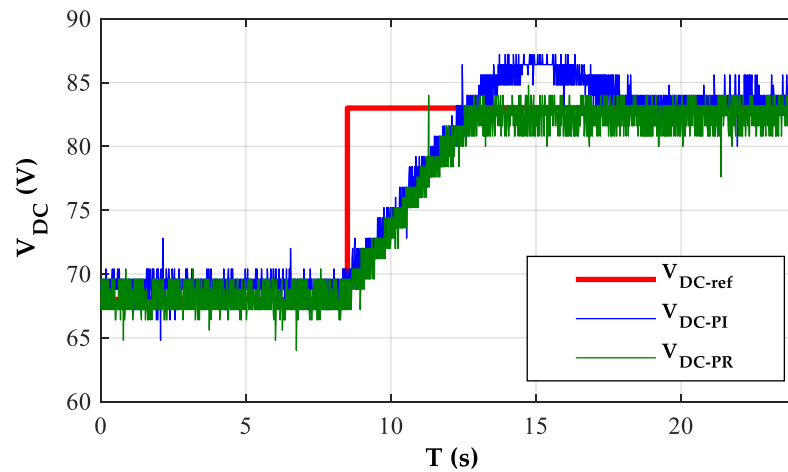


Figure 12. The experimental results of the voltage in the SRG power generation system under two controllers.

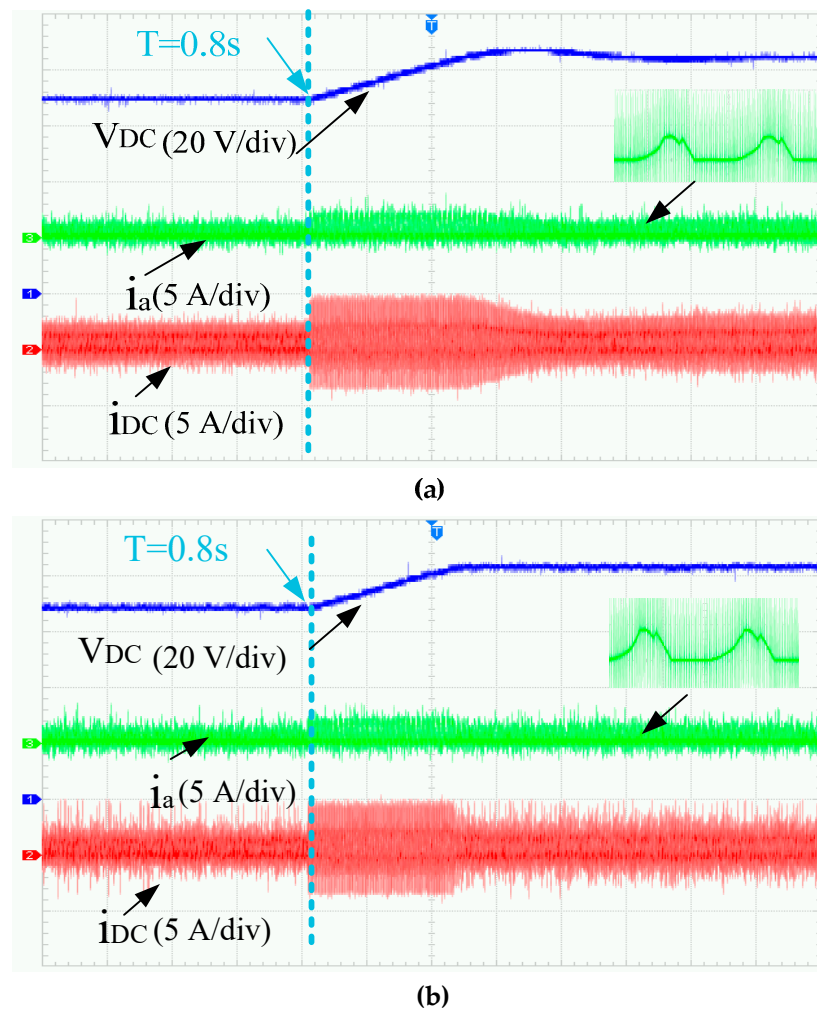


Figure 13. The experimental waveforms of SRG control with variable voltage: (a) the waveforms under PI controller; (b) the waveforms under PR controller.

It can be observed that the output voltage obtained by applying the PI control method requires about 0.92 s to reach a stable state. However, the output voltage obtained using the PR control method takes only about 0.52 s to reach a stable state. Consequently, the

system controlled by the PR method responds faster than the system controlled by the PI method. Furthermore, from Figure 12 and Table 4, we can also observe that V_{DC} has a larger overshoot when operated under PI control, but there is no overshoot of V_{DC} when operated under PR control at the startup phase. It can be seen from Table 4 that the ripple of V_{DC} is the smallest among the two controlled methods.

Table 4. Experimental results of the voltage step change.

Control Schemes	Rise Time (s)	Settling Time (s)	Peak Overshoot	Voltage Ripple (%)
PI	0.40	0.92	5.6	2.88
PR	0.22	0.52	0	2.85

In the case of SRG operations at wind speed step change, the generator speed changes from 500 to 1000 rpm at $T = 1$ s. The results of the output DC link voltage for each controller as a function of different generator speeds are presented in Figure 14. Good voltage control performance over a wide range of speed of SR power generator system for the two methods of control can be noticed. As described, the PR controller obtains higher dynamic performance compared to a conventional controller (PI). It allows the SRG to reach its reference voltage faster with no overshoot.

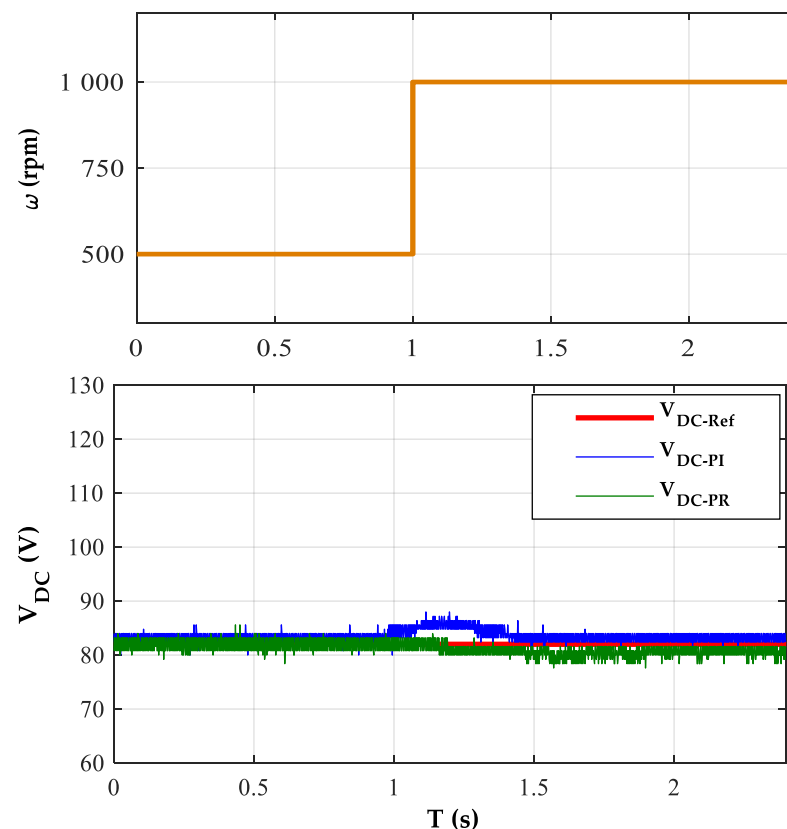


Figure 14. The experimental results of two methods controlling the SRG power generation system from 500 rpm to 1000 rpm.

Figure 15 shows the main experimental waveforms of the SR power generation system with the PI and PR controls. The winding phase current waveform is in a steady state with the maximum value of 3A for both controllers. As can be observed from Figure 14, compared to the traditional PI control, the voltage ripple in the case of PR control is similar but smaller at high speed (1000 rpm). At the low speed (500 rpm), I_a starts to increase since the two switches of the phase are turned off. When I_a becomes equal to I_{ref} , since the back

emf is lower than the DC link voltage, the hysteresis controller will be capable of regulating the current for the two-controller.

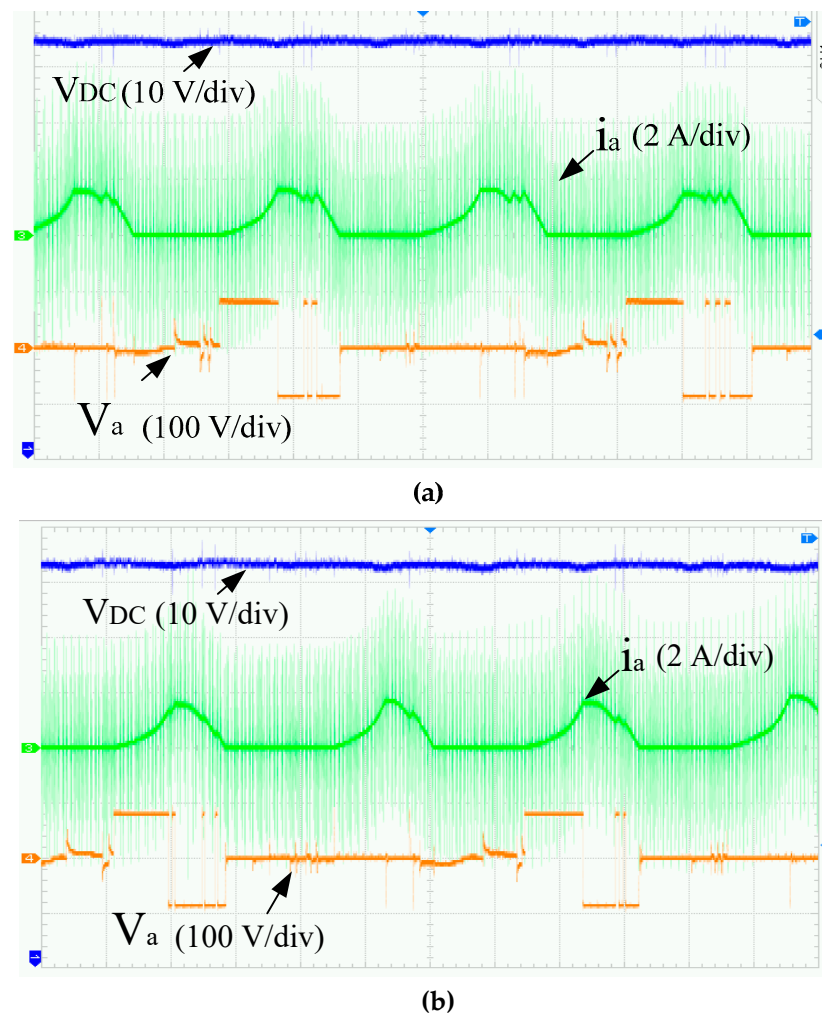


Figure 15. Experimental waveforms at 500 rpm of two controllers of SRG power system: (a) PI control; (b) PR control.

As shown in Figure 16, at the high speed (1000 rpm), I_a also starts to increase since the two switches of the phase are turned off. When i_a is equal to I_{ref} , the two switches of the phase are opened. As the back emf is greater than the DC link voltage at this point, the current continues to increase. Therefore, the hysteresis controller cannot regulate the current within the hysteresis band. The output of the hysteresis controller is, thus, a single pulse and the phase current I_a becomes much smoother, without chopping, for both controllers. To verify the PR and PI controllers for SR power generation when the inductance motor (IM) speed changes, the voltage reference is maintained at 83 V, and the speed changes from 500 to 800 rpm. The voltage is kept constant over the speed variations, allowing observation of the performance of the PR controller in the regulation of SR power generation as the speed of the IM changes, as in Table 5.

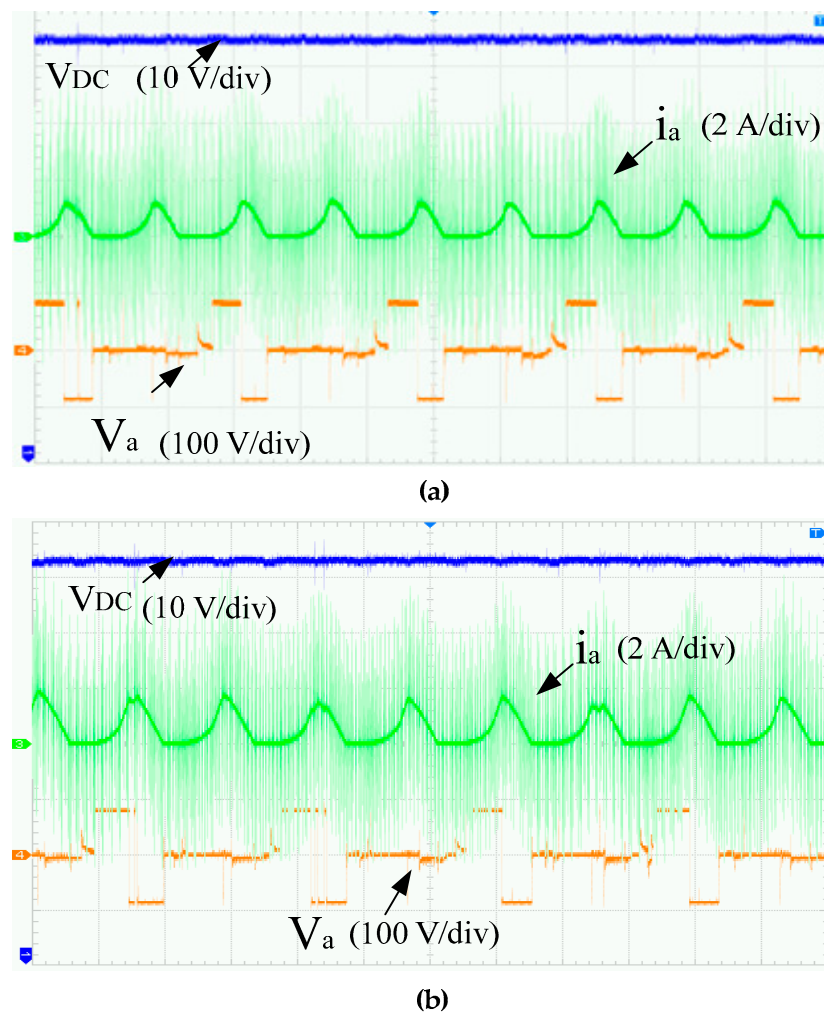


Figure 16. Experimental waveforms at 1000 rpm of two controllers of the SRG power system: (a) PI control; (b) PR control.

The rise time, the settling time, the peak overshoot, and the voltage ripple for each controller are illustrated in Table 5. Compared with the traditional PI control, the output voltage ripple when applying the PR control is smaller than the ripple under the traditional PI control at different speeds. It can be observed that the PR controller has better performance due to there being no overshoot in each condition. The fast response of the PR controller to reach a stable state compared with the PI control can also be noticed. Likewise, with the traditional PT control, the output voltage V_{DC} has a smaller overshoot with 3.8 at the startup phase in high speed, and 0.64 s is needed to reach the steady state, as shown in Table 5.

Table 5. Controllers’ performance for wind speed change operation.

	500 (rpm)		600 (rpm)		700 (rpm)		800 (rpm)	
	PI	PR	PI	PR	PI	PR	PI	PR
Rise time (s)	1.3	0.84	0.66	0.34	0.45	0.38	0.64	0.45
Settling time (s)	1.68	1.49	1.02	0.48	1	0.62	1.2	0.82
Peak overshoot	0.91	0	3.8	0	3.4	0	3.83	0
Voltage ripple (%)	4.7	4.5	4.28	3.8	3.06	2.79	3.58	3.4

6. Conclusions

A comparative study of two control laws based on PI and PR controllers for DC voltage control of SRG in wind application has been performed. The classical PI and the PR controller both generate the current setpoint for inner-current loop, and have been theoretically investigated and practically tested. In both cases, the solution presented was based on linearisation of the SRG model for a specific operating point, and then applying linear control techniques for simplification. The core version of the controller makes this understanding more transparent, focusing our attention on the essential action on the DC bus. The linear controllers sacrificed part of the dynamic performance in order to be easily adaptable and improve their steady-state performance. The experiment results showed that the proposed controllers operate stably and are reliable under different working conditions. Furthermore, the PR control, compared with the traditional PI controller method, had a rapid response during start-up and established a stable steady state. The rise time was reduced by 45% compared to the PI controller. Therefore, the PR control method has a better response capacity for variable wind speed when compared with the traditional PI. The ripple of the output voltage was also reduced with the PR control method.

Author Contributions: Conceptualization, Z.T., R.E.A. and A.K.; methodology, R.E.A. and A.K.; validation, Z.T., M.P., R.E.A. and A.K.; formal analysis, Z.T., R.E.A. and A.K.; investigation, Z.T., M.P., R.E.A. and A.K.; resources, Z.T. and R.E.A.; data curation, Z.T.; writing—original draft preparation, Z.T.; writing—review and editing, Z.T., M.P., R.E.A. and A.K.; supervision, R.E.A.; funding acquisition, A.K. All authors have read and agreed to the published version of the manuscript.

Funding: This study was financed in part by the University of Sousse, in part the participation of Manuel Pereira by National Funds through the Portuguese funding agency, FCT—Fundação para a Ciência e a Tecnologia, under Scholarship SFRH/BD/04583/2020. The participation of Rui Esteves Araújo in this work was financed by National Funds through the Portuguese funding agency, FCT—Fundação para a Ciência e a Tecnologia, within project UIDB/50014/2020.

Institutional Review Board Statement: Not applicable.

Informed Consent Statement: Not applicable.

Data Availability Statement: Not applicable.

Conflicts of Interest: The authors declare no conflict of interest.

References

1. Chen, Z.; Li, H. Overview of different wind generator systems and their comparisons. *IET Renew. Power Gener.* **2008**, *2*, 123–138. [[CrossRef](#)]
2. Liu, Y.; Ren, L.; Li, Y.; Zhao, X. The industrial performance of wind power industry in China. *Renew. Sustain. Energy Rev.* **2015**, *43*, 644–655. [[CrossRef](#)]
3. De Oliveira, A.L.; Capovilla, C.E.; Santana Casella, I.R.; Azcue-Puma, J.L.; Sguarezi Filho, A.J. Co-Simulation of an SRG Wind Turbine Control and GPRS/EGPRS Wireless Standards in Smart Grids. *IEEE/CAA J. Autom. Sin.* **2021**, *8*, 656–663. [[CrossRef](#)]
4. Gao, S.; Wang, Q.; Li, G.; Qian, Z.; Zhou, S.; Li, Z. A Deflectable Switched Reluctance Motor/Generator for Wave Energy Conversion and Underwater Propulsion Systems. *J. Electr. Eng. Technol.* **2021**, *16*, 3157–3167. [[CrossRef](#)]
5. Valdivia, V.; Todd, R.; Bryan, F.J.; Barrado, A.; Lazaro, A.; Forsyth, A.J. Behavioral Modeling of a Switched Reluctance Generator for Aircraft Power Systems. *IEEE Trans. Ind. Electron.* **2014**, *61*, 2690–2699. [[CrossRef](#)]
6. Zhu, Y.; Wu, H.; Zhang, J. Regenerative Braking Control Strategy for Electric Vehicles Based on Optimization of Switched Reluctance Generator Drive System. *IEEE Access* **2020**, *8*, 76671–76682. [[CrossRef](#)]
7. Diao, K.; Sun, X.; Lei, G.; Guo, Y.; Zhu, J. Multimode Optimization of Switched Reluctance Machines in Hybrid Electric Vehicles. *IEEE Trans. Energy Convers.* **2021**, *36*, 2217–2226. [[CrossRef](#)]
8. Sun, X.; Diao, K.; Yang, Z. Performance improvement of a switched reluctance machine with segmental rotors for hybrid electric vehicles. *Comput. Electr. Eng.* **2019**, *77*, 244–259. [[CrossRef](#)]
9. Bahy, M.; Nada, A.S.; Elbanna, S.H.; Shanab, M.A.M. Voltage control of switched reluctance generator using grasshopper optimization algorithm. *Int. J. Power Electron. Drive Syst.* **2020**, *11*, 75. [[CrossRef](#)]
10. Chen, H.; Xu, D.; Deng, X. Control for Power Converter of Small-Scale Switched Reluctance Wind Power Generator. *IEEE Trans. Ind. Electron.* **2021**, *68*, 3148–3158. [[CrossRef](#)]
11. Li, Z.; Yu, X.; Qian, Z.; Wang, X.; Xiao, Y.; Sun, H. Generation Characteristics Analysis of Deflection Type Double Stator Switched Reluctance Generator. *IEEE Access* **2020**, *8*, 196175–196186. [[CrossRef](#)]

12. Sarr, A.; Bahri, I.; Berthelot, E.; Kebe, A.; Diallo, D. Switched Reluctance Generator for Low Voltage DC Microgrid Operation: Experimental Validation. *Energies* **2020**, *13*, 3032. [[CrossRef](#)]
13. dos Santos Barros, T.A.; dos Santos Neto, P.J.; Nascimento Filho, P.S.; Moreira, A.B.; Ruppert Filho, E. An approach for switched reluctance generator in a wind generation system with a wide range of operation speed. *IEEE Trans. Power Electron.* **2017**, *32*, 8277–8292. [[CrossRef](#)]
14. Araujo, W.R.H.; Reis, M.R.C.; Wainer, G.A.; Calixto, W.P. Efficiency Enhancement of Switched Reluctance Generator Employing Optimized Control Associated with Tracking Technique. *Energies* **2021**, *14*, 8388. [[CrossRef](#)]
15. Lu, M.Z.; Jhou, P.H.; Liaw, C.M. Wind Switched-Reluctance Generator Based Microgrid with Integrated Plug-In Energy Support Mechanism. *IEEE Trans. Power Electron.* **2021**, *36*, 5496–5511. [[CrossRef](#)]
16. Zan, X.; Ni, K.; Zhang, W.; Jiang, Z.; Cui, M.; Yu, D.; Zeng, R.A. New Control Strategy for SR Generation System Based on Modified PT Control. *IEEE Access* **2019**, *7*, 179720–179733. [[CrossRef](#)]
17. Chirapo, K.A.C.; Oliveira, A.L.; Sguarezi Filho, A.J.; Pelizari, A.; Di Santo, S.G.; Costa, E.C.M. P+RES Controller Applied to the Direct Power Control of Switched Reluctance Generator. *J. Control Autom. Electr. Syst.* **2020**, *31*, 360–366. [[CrossRef](#)]
18. Touati, Z.; Pereira, M.; Araújo, R.E.; Khedher, A. Improvement of Steady State Performance of Voltage Control in Switched Reluctance Generator: Experimental Validation. *Machines* **2022**, *10*, 103. [[CrossRef](#)]
19. Chen, H.; Gu, J.J. Implementation of the Three-Phase Switched Reluctance Machine System for Motors and Generators. *IEEE/ASME Trans. Mechatron.* **2010**, *15*, 421–432. [[CrossRef](#)]
20. Hao, C.; Xianjun, M.; Fang, X.; Tao, S.; Guilin, X. Fault tolerant control for switched reluctance motor drive. In Proceedings of the IEEE 2002 28th Annual Conference of the Industrial Electronics Society, IECON 02, Sevilla, Spain, 5–8 November 2002; Volume 2, pp. 1050–1054. [[CrossRef](#)]
21. Touati, Z.; Mahmoud, I.; Khedher, A. Hysteresis Current Control of Switched Reluctance Generator. In Proceedings of the 2020 11th International Renewable Energy Congress (IREC), Hammamet, Tunisia, 29–31 October 2020; pp. 1–8. [[CrossRef](#)]
22. Sunan, E.; Syed Muhammad Raza, K.; Goto, H.; Guo, H.-J.; Ichinokur, O. Instantaneous torque ripple control and maximum power extraction in a permanent magnet reluctance generator driven wind energy conversion system. In Proceedings of the XIX International Conference on Electrical Machines—ICEM 2010, Rome, Italy, 6–8 September 2010; pp. 1–6. [[CrossRef](#)]
23. Ramu, K. *Switched Reluctance Motor Drives: Modeling, Simulation, Analysis, Design, and Applications*; CRC Press: Boca Raton, FL, USA, 2011.
24. Yepes, A.G.; Freijedo, F.D.; Doval-Gandoy, J.; Lopez, O.; Malvar, J.; Fernandez-Comesana, P. On the discrete-time implementation of resonant controllers for active power filters. In Proceedings of the 35th Annual Conference of IEEE Industrial Electronics, Porto, Portugal, 3–5 November 2009. [[CrossRef](#)]